Systems/Circuits

Vigilance and Behavioral State-Dependent Modulation of Cortical Neuronal Activity throughout the Sleep/Wake Cycle

Aurélie Brécier,[1] Mélodie Borel,[1] Nadia Urbain,[2] and Luc J. Gentet[1]

[1]Integrated Physiology of Brain Arousal Systems, and [2]Physiopathology of Sleep Networks, Lyon Neuroscience Research Center, Institut National de la Santé et de la Recherche Médicale U1028–Centre National de la Recherche Scientifique Mixed Research Unit 5292, Université Claude-Bernard Lyon 1, 69372 Lyon, France

GABAergic inhibitory neurons, through their molecular, anatomic, and physiological diversity, provide a substrate for the modulation of ongoing cortical circuit activity throughout the sleep/wake cycle. Here, we investigated neuronal activity dynamics of parvalbumin (PV), vasoactive intestinal polypeptide (VIP), and somatostatin (SST) neurons in naturally sleeping head-restrained mice at the level of layer 2/3 of the primary somatosensory barrel cortex of mice. Through calcium imaging and targeted single-unit loose-patch or whole-cell recordings, we found that PV action potential firing activity was largest during both rapid eye movement (REM) and nonrapid eye movement (NREM) sleep stages, that VIP neurons were most active during REM sleep, and that the overall activity of SST neurons remained stable throughout the sleep/wake cycle. Analysis of neuronal activity dynamics uncovered rapid decreases in PV cell firing at wake onset followed by a progressive recovery during wake. Simultaneous local field potential (LFP) recordings further revealed that except for SST neurons, a large proportion of neurons were modulated by ongoing delta and theta oscillations. During NREM sleep spindles, PV and SST activity increased and decreased, respectively. Finally, we uncovered the presence of whisking behavior in mice during REM sleep and show that the activity of VIP and SST is differentially modulated during awake and sleeping whisking bouts, which may provide a neuronal substrate for internal brain representations occurring during sleep.

Key words: calcium imaging; cortex; electrophysiology; interneuron; sleep; somatosensory

---

Significance Statement

In the sensory cortex, the balance between excitation and inhibition is believed to be highly dynamic throughout the sleep/wake cycle, shaping the response of cortical circuits to external stimuli while allowing the formation of newly encoded memory. Using *in vivo* two-photon calcium imaging or targeted single-unit recordings combined with LFP recordings, we describe the vigilance state and whisking-behavior-dependent activity of excitatory pyramidal and inhibitory GABAergic neurons in the supragranular layers of mouse somatosensory cortex. Interneuronal activity was found to be differentially modulated by ongoing delta and theta waves, sleep spindles, and a novel type of whisking observed during REM sleep, potentially providing a neuronal substrate for internal brain representations occurring during sleep.

Introduction

The sleep/wake cycle is characterized by specific patterns of cortical activity, high-frequency and low-amplitude activity during both wake and rapid-eye movement (REM) sleep and high-amplitude, low-frequency EEG activity in nonrapid eye movement (NREM) sleep. Several hypotheses have emerged on the function of sleep, with evidence pointing to its role in memory consolidation (Born et al., 2006; Girardeau et al., 2009; Vaz et al., 2020). Indeed, delta (1–4 Hz) and spindles (10–17 Hz) oscillations are well-known hallmarks of NREM sleep supporting memory formation and consolidation (Steriade and Timofeev, 2003; Maingret et al., 2016; Ulrich, 2016; Latchoumane et al., 2017), whereas theta activity (5–9 Hz) is a marker of exploratory behavior and of REM sleep in rodents (Buzsáki, 2002; Montgomery et al., 2008; Girardeau et al., 2009). It is clear that the internal brain state and the way sensory cortex processes information are dramatically altered during these vastly different vigilance states, but the underlying circuit mechanisms remain poorly understood.

Cortical networks are composed of both excitatory projection neurons and local inhibitory interneurons, which represent a sparse yet diverse family of GABAergic neurons with different

morphologies and electrophysiological properties (Markram et al., 2004; Tremblay et al., 2016) and are associated with distinct functional roles in local cortical circuits (Atallah et al., 2012; Gentet et al., 2012; Lee et al., 2013). Despite this diversity, the following three main subtypes of interneurons have been identified in the past decade: parvalbumin (PV)-containing neurons, inhibiting pyramidal (PYR) cells soma, and vasoactive intestinal peptide (VIP)-expressing and somatostatin (SST)-expressing cells, inhibiting, respectively, other interneurons and distal part of excitatory cells. Although there is accumulating evidence that the firing rate of pyramidal cells evolves over the time course of the sleep/wake cycle (Hobson and McCarley, 1971; Steriade et al., 2001; Watson et al., 2016; Miyawaki et al., 2019), changes in the activity of these three subtypes of interneurons remain unclear.

Recent studies have nevertheless revealed brain state-dependent modulation of neocortical interneuron firing activity in different brain regions, notably in the primary somatosensory (S1) barrel cortex during active whisking (Gentet et al., 2010, 2012; Lee et al., 2013; Muñoz et al., 2017). In the motor cortex, additional evidence points toward a vigilance state-dependent of modulation of PV neurons throughout the sleep/wake cycle (Niethard et al., 2016, 2021), whereas SST neurons in the frontal cortex have been shown to be strongly phase locked to local slow-wave sleep oscillations (Funk et al., 2017). In addition, multiunit recordings revealed changes in the firing rates of fast-spiking, putative PV cells during NREM and REM sleep in rodents (Vyazovskiy et al., 2009; Vijayan et al., 2010; Watson et al., 2016; Miyawaki et al., 2019) and humans (Peyrache et al., 2011). Finally, a recent study highlighted that acetylcholine and serotonin could both directly modify firing patterns of S1 VIP neurons (Prönneke et al., 2020; Gasselin et al., 2021).

Two main sleep hypotheses have emerged concerning the impact of sleep on neuronal network excitability; (1) the synaptic downscaling homeostasis hypothesis proposes that the overall neuronal excitability is reduced during sleep via widespread synaptic downscaling (Tononi and Cirelli, 2009; Cirelli, 2017), and (2) the active system consolidation hypothesis proposes that memory consolidation in the neocortex is achieved through neuronal replay linked to hippocampal activity and long-term synaptic plasticity occurring throughout NREM sleep (Frankland and Bontempi, 2005; Born, 2006; Klinzing et al., 2019). GABAergic interneurons, through their cell-type- and compartment-specific postsynaptic targeting, would play central roles in both processes.

To better understand how the activity of different neurons within a local cortical network evolve on a temporally fine scale and in relation to the phases of ongoing local oscillations occurring throughout the sleep/wake cycle, we characterized the activity of the three main subtypes of GABAergic neurons involved in regulating the local excitatory-inhibitory balance in layer 2/3 of S1 in naturally sleeping, head-restrained mice either by using calcium imaging or by targeting PV, VIP, and SST neurons under two-photon microscopy visual guidance (Margrie et al., 2003). Both techniques uncovered cell-type differences and vigilance-state-specific differences in neuronal activity, and their results converge to show increased PV cell activity during NREM and REM sleep, increased VIP cell activity specifically during REM sleep, but an overall stable activity of SST neurons throughout the sleep/wake cycle. Further state-, whisking- and oscillation-dependent shifts in firing patterns and action potential (AP) firing frequencies revealed the important regulatory role played by GABAergic cells throughout the various stages of the sleep/wake cycle.

Materials and Methods

Transgenic mice. To record local cortical neuronal activity across the sleep/wake cycle, transgenic mouse lines where a red fluorophore could be expressed in genetically identified subpopulations of GABAergic neurons were used (Taniguchi et al., 2011). Heterozygous male offsprings of *GAD2-IRES-Cre* driver mice (catalog #010802, The Jackson Laboratory) crossed with Ai32(RCL-ChR2(H134R)/EYFP) reporter mice (catalog #012569, The Jackson Laboratory) were chosen for our experiments.

All animal experiments were conducted after approval by the local ethical committee of the University of Lyon and the Ministry of Science (Protocol number APAFIS 4613) in accordance with European Union Directive 86/609/EEC on the protection of animals used for experimental and other scientific purposes. All animals used in this study were maintained on a C57Bl6 genetic background and group housed in the vivarium under normal light/dark conditions.

We used heterozygous 6–12-week-old male and female offsprings of either *PV-IRES-Cre* mice (catalog #008069), *VIP-IRES-Cre* (catalog #010908), or *SST-IRES-Cre* (catalog #013044) driver mice crossed with *Ai9 loxP-tdTomato* reporter mice (catalog #007909), all from The Jackson Laboratory. Fifteen and 60 mice were used in total for the calcium imaging and patch-clamp studies, respectively (Extended Data Figs. 1-1, 2-1). Experiments were performed during the light period of the 12 h light/dark cycle. All surgical procedures were performed under isoflurane anesthesia (4% induction, 1.5–2% maintenance). A subcutaneous injection of carprofen (5 mg/kg) and dexamethasone (0.08 mg) was administered before surgery to reduce pain and swelling.

First, animals were implanted with a lightweight head bar allowing head restraint under two-photon microscopy. The recording chamber was positioned above S1 barrel cortex (−2 mm posterior to bregma and −3.5 mm lateral to midline). Stainless steel screws and wires were inserted respectively over the contralateral skull (frontal electrode, +2 mm anterior to bregma, +2 mm lateral; parietal electrode, −2 mm posterior to bregma, +2 mm lateral) and into the neck muscles for monitoring of EEG and EMG. The skull positions for the EEG screws were chosen to facilitate NREM sleep detection (Fang et al., 2009). After recovery from surgery, mice were habituated to the head restraint for 3 weeks (daily sessions of increasing duration) until regular bouts of NREM and REM sleeps were detected.

Three days after implantation for the calcium imaging study and on the first day of recordings for the patch-clamp study, mice were anesthetized with ~1.5% isoflurane, and the C2 barrel column of the primary S1 cortex was located on the skull using intrinsic optical imaging (QImaging). In short, all whiskers contralateral to the metal head holder chamber were removed except for C2. The skull thickness under the chamber was softly reduced with a dental drill, and a drop of ASCF was placed inside the chamber. The C2 whisker was deflected at 8 Hz, with an amplitude of 5° for 5 s. Successive trials of stimulation were succeeding by trials with no stimulation. Images were processed and analyzed using V++ software (Digital Optics). The evoked hemodynamic signal was imaged under red LED (610 nm) by subtracting nonstimulation trials from stimulation trials. Finally, the combination of the picture taken under white light and the one taken under red LED allowed the targeting of C2 column position inside the chamber (Bouchard et al., 2009).

Virus injection. For the calcium imaging study, animals were injected with a GCamP6m (AAV1.Syn.GCaMP6m.WPRE.SV40, Penn Vector Core; Chen et al., 2013), under isoflurane anesthesia at 1.5–2%, following the intrinsic optical imaging session. A small craniotomy (diameter 100 μm) was drilled 500 μm lateral to the identified C2 column, and the pia was removed. An injection at 150–300 μm depth was performed with a glass pipette inclined at 30° and filled with the virus (0.50 nl/min, 1 μl delivered in total).

At the end of the habituation period, a small craniotomy (centered on C2 column (~1 × 2 mm) was performed above the C2 barrel column. Dura mater was removed, and 1.5% agarose was applied onto the cortical surface to stabilize it. For the calcium imaging study, a coverslip of the precise dimension of the craniotomy was glued on the skull (Goldey et al., 2014). For patch-clamp experiments, an opening was left on one side of the craniotomy for pipette insertions. The exposed brain was continually immersed in ASCF. Animals were allowed to recover for

at least 2–3 h before recording, and recording sessions lasted up to 4 h. Animals were placed on the stage of a LaVision Two-Photon Microscope combined with a pulsed Chameleon Ti-Sapphire laser (λ = 920 nm, Coherent). Image and data acquisition was obtained using ImSpector Pro (LaVision). Simultaneous local field potential (LFP) and whole-cell/cell-attached recordings were performed using glass micropipettes filled with ACSF containing the following (in mM): 135 NaCl, 5 KCl, 5 HEPES, 1 $MgCl_2$, 1.8 $CaCl_2$, and 0.01 Alexa-488 (adjusted to pH 7.3 with NaOH) and an internal solution containing the following (in mM): 135 potassium gluconate, 4 KCl, 10 HEPES, 10 phosphocreatine, 4 MgATP, 0.3 Na_3GTP, and 0.01 Alexa 488 (adjusted to pH 7.3 with KOH; osmolarity adjusted to 300 mOsmol).

Calcium imaging . Images (256 × 91 pixels, 1 pixel = 1.76 μm^2) were acquired at a frequency of 10.12 Hz. Calcium imaging videos were composed of 1200, 1800, or 2400 images, corresponding to recordings of ~2, 3, or 4 min, respectively, chosen to minimize potential bleaching and maximize the chances of obtaining bouts of NREM and REM sleep and wakefulness. A custom-made MATLAB routine (Jorrit Montijn, Universiteit van Amsterdam and Mélodie Borel, Université Claude Bernard de Lyon) was used to quantify the GCaMP6-related fluorescence variations of neurons. In short, small *x–y* drifts were corrected with an image registration algorithm. If a substantial *z* drift was detected during a session, that session was rejected and removed from further analysis. Regions of interest (neuronal somat and neuropil) were determined semiautomatically using our custom-made MATLAB software, and ΔF/F0 values for all neurons were then calculated as follows: fluorescence (F) of each neuron was normalized by the baseline fluorescence of that neuron (F0), taken as the mean of the lowest 50% fluorescence for that session (ΔF = (F − F0)/F0; adapted from Goltstein et al., 2013). Neurons that were also expressing TdTomato were subsequently categorized as PV, VIP, or SST cells, whereas all other neurons were considered to be putative excitatory pyramidal cells.

Patch-clamp/LFP recordings. Glass pipettes (open tip resistances, 3–4 MOhms for LFP pipettes, 4–6 MOhms for loose-patch or whole-cell patch-clamp pipettes) were lowered into the C2 column of S1 barrel cortex under positive pressure, using two micromanipulators (Scientifica PatchStar). Once a neuron of interest was identified in the field of view, the LFP pipette was positioned nearby (~100–200 μm away). Loose-patch recordings were obtained by approaching the neuron under low pressure until the open tip resistance increased to ~100 MOhms. Whole-cell recordings were obtained by perforating the membrane through rapid suction after obtaining a gigaohm seal; *z*-stack images were performed to confirm the position of the pipette tip relative to the neuron of interest. Signals were acquired at 20 kHz and low-pass Bessel filtered at 8 kHz with a MultiClamp 700B amplifier (Molecular Devices). Spikes were automatically detected using a manually set threshold on the derivative of the signal.

Oscillatory bouts (delta oscillations, 1–4 Hz; theta oscillations, 5–9 Hz; spindles, 10–17 Hz) were detected using scripts adapted from the Freely Moving Animal (FMA) MATLAB toolbox (developed by Michaël Zugaro, Collège de France). After bandpass filtering, the LFP signal in the appropriate frequency range, a low-pass filtered squared envelope of the *z*-scored signal was computed. Only bouts that crossed the threshold of *z* = 2, contained a peak of at least *z* = 5, and lasted at least 250 ms and 110 ms for delta and theta oscillations, respectively, were considered. Bouts were further merged if separated by <500 ms. Finally, only episodes lasting over 1 s for delta and 350 ms for theta, corresponding to a minimum of three oscillations per bout, were kept. Spindles were detected by filtering LFP signal between 10 and 17 Hz, and the same low-pass filtered as previously described has been computed. Any event has to cross a threshold of *z* = 2.5 with a minimum peak of *z* = 4. Too-close events (<200 ms) were merged. Finally, only events lasting over 500 ms and <3.5 s were kept. Delta events preceding spindles were first semiautomatically detected on the LFP signal filtered between 0.5 and 4 Hz and *z*-scored using the FMA MATLAB toolbox. Events crossing a threshold of *z* = 1.5 with a minimum peak of *z* = 2 were subsequently manually selected. Indeed, delta events, as defined by us (Urbain et al., 2019) and previously (Todorova and Zugaro, 2019),

present a characteristic shape that is different from delta oscillations, roughly consisting of a half oscillatory delta UP cycle. Delta events had to last between 100 and 800 ms and had to occur within the 250 ms preceding the spindles. Finally, for the analysis of neuronal activity during delta–spindles bouts, the peak of the delta event was used to align all traces.

On each detected oscillation, a Hilbert transform was applied, and the phase of each spike relative to the oscillation was computed. Only cells with >30 spikes detected on oscillations were taken into account for this analysis. All circular statistics were performed using the Circular Statistics Toolbox developed for MATLAB (Berens, 2009). First, a circular test (Rayleigh's test) was performed to determine whether cells were significantly modulated by the oscillation ($p < 0.01$). Then a Von Mises distribution was fitted on each spike distribution of modulated cells, and two parameters were extracted, the preferred phase (μ) and the concentration (κ). The Von Mises μ corresponds to the mean location of the peak of the distribution, whereas the Von Mises κ estimates how much the distribution is concentrated on μ.

Sleep scoring and whisker tracking. EEG and EMG signals were recorded at 20 kHz, amplified (Model 3000 AC/DC, A-M Systems) and bandpass filtered (EEG, 0.1–100 Hz; EMG, 300–3000 Hz) for online display during recording sessions. Sleep scoring was performed manually off-line with at a temporal precision of 100 ms. Parameters used to help in the identification of the three discrete vigilance states (Wake, NREM, and REM) were EEG and EMG variance, theta/delta ratio and an ongoing fast Fourier transform (FFT). Wake episodes were defined by a low EEG variance and a high EMG variance. NREM sleep bouts were determined based on a lower EMG and higher EEG variance, together with the presence of spindles on the EEG and/or the LFP. REM sleep was scored when a high theta/delta ratio was observed on the EEG, accompanied by a very low EMG variance. Episodes with undefined vigilance states, such as transitional and intermediate states or episodes lasting <20 s, were removed from the analysis. Whisker movement was tracked with a high speed (320 × 240 pixels; 100 Hz) camera (Redlake MotionPro camera under infrared illumination, λ 850 nm; OPT Machine Vision). The angle of whisker deflection was calculated using custom-made software written in MATLAB (courtesy of Paul-Antoine Libourel). An episode of free whisking was considered as such if the C2 whisker deflection exceeded 20° and contained at least three protraction/retractions exceeding 10°, lasting at least 200 ms. Twitches were also detected (>20° but less than three protraction/retractions exceeding 10° detected) and were removed from the analysis of wakefulness without whisking. Under these conditions, free whisking episodes were detected in both Wake and REM sleep but not during NREM sleep.

Statistics. All classical statistical analysis was performed using routine functions in MATLAB. Normality distribution and homoscedasticity was checked on samples using the Kolmogorov–Smirnov and Levene's tests, respectively. In each case, samples were nonparametric, and medians plus or minus median absolute deviations are reported below in Results. A Wilcoxon signed-ranked test and a Friedman test were applied for two-paired groups and multiple group comparison, respectively (unless otherwise stated). If compared samples were considered to be independent, a Mann–Whitney test for two-group comparison or a Kruskal–Wallis test for multiple group comparison was conducted. Finally, when multiple group comparisons appeared significantly different, corrected Wilcoxon sign-ranked and corrected Mann–Whitney tests were performed two by two for paired and independent data, respectively. For patch-clamp experimental data, some neurons were only recorded in a subset of the three main vigilance states (e.g., wakefulness and NREM sleep but not REM sleep). Therefore, samples were analyzed with a linear mixed-effects model (LMM) in R studio using the lme4 package and Satterthwaite approximation (Bates et al., 2015). For a better fit to data, repeated measurements were included. In this case, the estimate means and SEs, computed by a Kenward–Roger approximation are provided below in Results. Statistical significance is denoted by asterisks as follows: *$p < 0.05$, **$p < 0.01$, ***$p < 0.001$. All mice were used for each analysis (calcium imaging study, $n = 15$ mice; patch-clamp study, $n = 60$ mice).

Results

Cell-specific and vigilance-state-dependent calcium activity throughout the sleep/wake cycle

We first investigated how the activity of excitatory and inhibitory neurons might evolve throughout the sleep/wake cycle using *in vivo* two-photon calcium imaging. Transgenic mice expressing Cre tdTomato in either PV, VIP, or SST cells were injected with a calcium indicator (AAVsyn-GCaMP6m), allowing us to specifically identify and measure fluorescence changes in both interneurons and putative pyramidal cells in layers 2/3 of S1 barrel cortex (Fig. 1*A,B*). In total, 2338 putative pyramidal (i.e., neurons unlabeled with TdTomato) 310 PV, 113 VIP, 184 SST cells were recorded but only 1206 putative pyramidal, 164 PV, 78 VIP, and 134 SST were recorded in all three main vigilance states of the sleep/wake cycle and considered for analysis (Wake, NREM sleep, and REM sleep, $n = 15$ mice; Extended Data Fig. 1-1). Overall, we observed subtype-specific changes in activity throughout the different vigilance states (Fig. 1*C*). Notably, PV activity increased during sleep stages compared with wake ($\Delta F/F0$: Wake, $11.9 \pm 8.0\%$; NREM, $18.1 \pm 9.1\%$; REM, $20.2 \pm 10.6\%$, $n = 164$; $p < 0.001$ for Wake vs NREM and Wake vs REM), and the activity of VIP cells was significantly larger in REM sleep compared with NREM ($\Delta F/F0$: Wake, $37.4 \pm 22.9\%$; NREM, $25.6 \pm 14.3\%$; REM, $57.1 \pm 34.9\%$, $n = 78$; $p < 0.001$ for NREM vs REM). The average activity of both putative PYR and GABAergic SST neurons, however, remained unchanged throughout the sleep/wake cycle (Fig. 1*C,D*). Subdividing the population of PYR neurons into sextiles based on their average activity during wake revealed a larger activity variance during REM compared with wake and NREM sleep (σ, Wake = 70.1; NREM = 70.6; REM = 79.7; Levene's test $p < 0.001$; Fig. 1*D*). This observation prompted us to separate PYR neurons into two groups based on their average activity during REM sleep. High REM activity PYR displayed significantly lower activity in wake and NREM sleep ($\Delta F/F0$: Wake, $52.2 \pm 28.3\%$; NREM, $47.3 \pm 25.1\%$; REM, $71.2 \pm 27.0\%$, $n = 603$; $p < 0.001$ for both Wake vs REM and NREM vs REM), whereas low REM activity PYR cells showed increased wake and NREM activity ($\Delta F/F0$: Wake, $25.3 \pm 11.6\%$; NREM, $25.3 \pm 11.1\%$; REM, $18.3 \pm 7.5\%$, $n = 603$; $p < 0.001$ for both Wake vs REM and NREM vs REM; Fig. 1*E*). Furthermore, the average wake and NREM activity of high REM activity PYR cells was larger than their low REM activity counterparts (Mann–Whitney test, $p < 0.001$; Fig. 1*E*).

Next, we decided to examine the dynamics of calcium activity around vigilance state transitions. Transitions between vigilance states were manually detected and aligned at $t = 0$ s (Fig. 1*F*). Awakenings from both NREM and REM sleep stages provide a good temporal resolution through abrupt increases in EMG activity. Although the transition between NREM and REM sleep is often considered progressive, we were able to time stamp it when clear theta waves began to appear on the EEG, concomitant with a rapid reduction in EMG activity and the appearance of heartbeats in 92% of cases (Fig. 1*F*). The mean calcium activity between –10 and 0 s from the transition was compared with the activity between 0 to +10 s. We found that calcium activity of PV and VIP cells decreased and increased, respectively, at NREM to wake onsets (PV: NREM to Wake transitions, $15.1 \pm 11.1\%$ vs $10.4 \pm 8.2\%$, $n = 217$ cells, $p < 0.001$; VIP: NREM to Wake transitions, $16.0 \pm 14.5\%$ vs $26.6 \pm 19.6\%$, $n = 75$ cells, $p = 0.004$). In addition, PV neurons activity also decreased at wake onset after an REM episode, whereas VIP cell calcium fluorescence increased at REM onset (PV: REM to Wake transitions, $9.3 \pm 15.3\%$ vs $-1.3 \pm 12.3\%$, $n = 161$ cells, $p < 0.001$; VIP:

NREM to REM transitions, $16.8 \pm 22.5\%$ vs $39.0 \pm 40.3\%$, $n = 58$ cells, $p = 0.003$; Fig. 1*F*). These results could be reproduced using longer transition periods (± 30 s; data not shown). Although there were no significant changes in calcium fluorescence in both SST and PYR neurons around any state transition (as in Fig. 1*F*), additional analysis with longer transitions periods (± 30 s) revealed a significant decrease of SST neurons activity after REM onset (data not shown; NREM to REM transitions, $25.6 \pm 18.6\%$ vs $11.9 \pm 14.2\%$; $n = 32$, $p = 0.002$). Together, our results suggest that changes in vigilance states occurring throughout the sleep/wake cycle can lead to rapid alterations of layer 2/3 barrel cortex circuit dynamics subserved by local PV and VIP cells and to a lesser extent by SST.

Vigilance-state-dependent modulation of GABAergic neurons firing activity

Although the dynamics of calcium fluorescence across the sleep/wake cycle are a good indicator of overall activity changes, their temporal resolution remains limited. To better understand the circuit activity changes induced by different brain vigilance states, we next performed targeted loose- and whole-cell patch-clamp recordings of genetically identified PV, VIP, and SST neurons, as well as putative excitatory pyramidal cells under two-photon microscopy (PV loose patch $n = 32$, whole cell $n = 3$; VIP loose patch, $n = 31$, whole cell $n = 3$; SST loose patch $n = 32$, whole cell $n = 5$ including one silent; PYR loose patch $n = 18$, whole cell $n = 4$ including one silent; Fig. 2*A,B*) while simultaneously recording the local field potential (LFP) with a second glass pipette positioned in layer 2/3 of the C2 barrel column. In the next section, estimated means plus or minus estimated SEMs are stated, and firing activity was compared over the three vigilance states using LMM (see above, Materials and Methods).

AP firing activity of PV cells increased in NREM compare to Wake ($p < 0.001$) and increased in REM sleep compared with both Wake ($p < 0.001$) and NREM ($p = 0.003$; Wake, 15.0 ± 3.0 Hz, $n = 34$; NREM, 25.0 ± 3.0 Hz, $n = 35$; REM, 29.0 ± 3.2 Hz, $n = 31$; LMM; Fig. 2*C*). Firing rates of VIP cells significantly increased during REM sleep compared with NREM ($p = 0.002$), mirroring our results found under calcium imaging (Wake, 11.9 Hz ± 1.4, $n = 31$; NREM, 10.9 Hz ± 1.4, $n = 31$; REM, 13.3 Hz ± 1.5, $n = 28$; LMM). Finally, the AP firing activity of SST cells remained unchanged overall across vigilance states. For PYR neurons, we split our populations into two groups, as previously described, after removing a subset of cells that were not recorded during REM sleep ($n = 18$ cells). On average, high REM activity PYRs were less active in Wake compared with NREM and REM (Wake, 3.1 ± 0.6 Hz, $n = 9$; NREM, 4.9 ± 0.7 Hz, $n = 9$; REM, 6.8 ± 0.9 Hz, $n = 9$; $p < 0.001$ for Wake vs NREM, $p < 0.001$ for Wake vs REM, $p = 0.007$ for REM vs NREM; LMM), whereas low REM activity PYR cells did not display any significant changes in overall AP firing activity across vigilance (Fig. 2*C*). The activity of these two subgroups of PYR neurons was also consistently significantly different across all vigilance states (Mann–Whitney test, $p < 0.001$ for Wake, NREM, and REM; Fig. 2*C*). Together, these findings are consistent with our calcium activity results (Fig. 1), and confirm that PV cell activity increases during NREM and REM sleep compared with Wake, that VIP activity specifically increases during REM sleep compared with NREM, and that SST neuronal activity is overall not affected by the different stages of the sleep/wake cycle.

As for our calcium imaging study, we were able to manually time stamp clear transition points between vigilance states, both
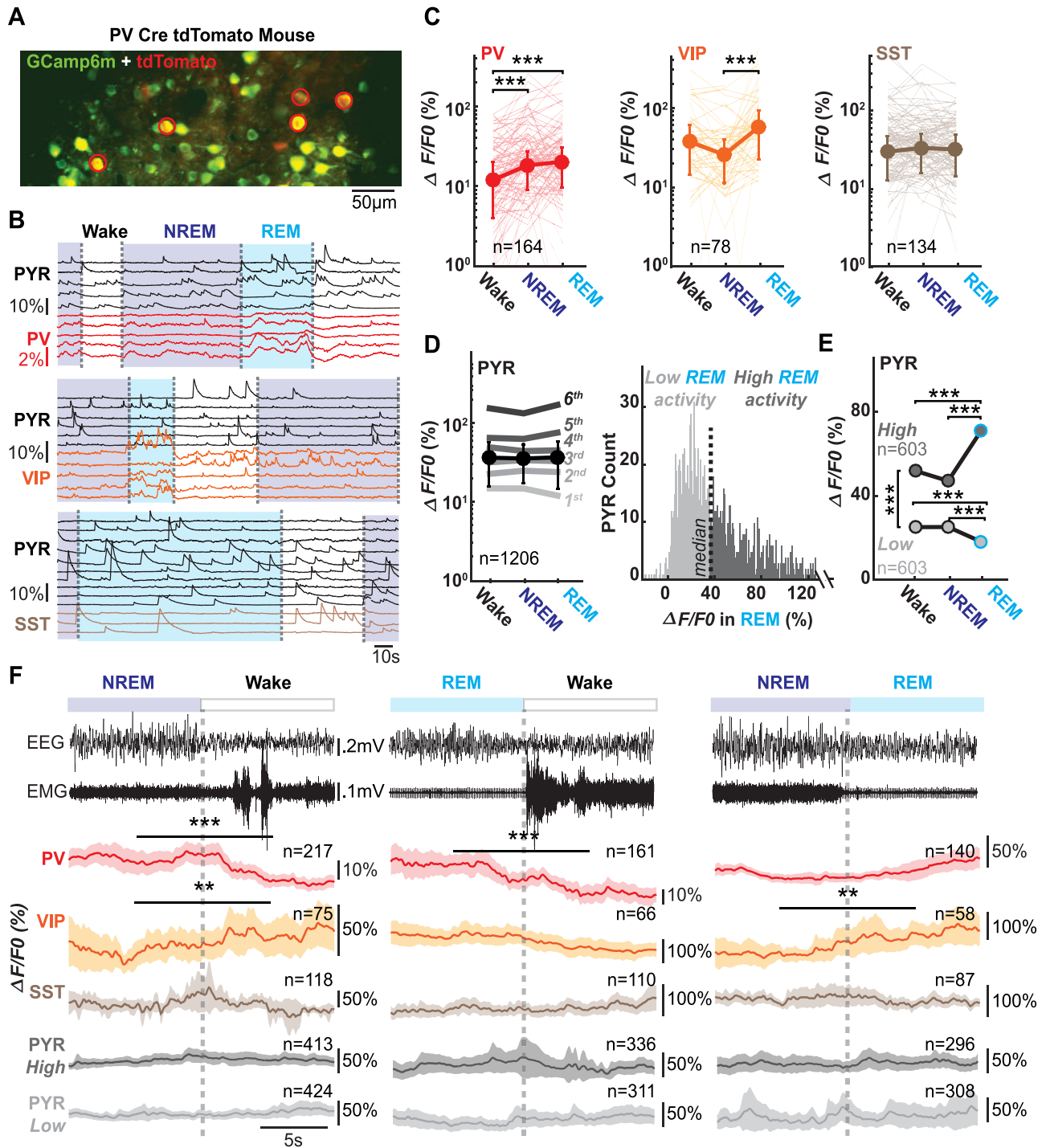
Figure 1. Calcium fluorescence activity changes across the sleep/wake cycle for pyramidal cells and interneurons. ***A***, Example of a recording field in layers 2/3 of barrel cortex in a PV Cre-tdTomato mouse. All neurons in green express GCaMP6m, whereas PV neurons express, in addition, tdTomato in red. PV cells expressing both red and green fluorescences are marked by a red circle. ***B***, Changes in GCaMP6m fluorescence across time and vigilance states for each detected neuron in one recording field. Example calcium traces in a PV Cre-tdTomato (top, same as in ***A***), a VIP Cre-tdTomato (middle), and in a SST Cre-tdTomato mouse (bottom). ***C***, Median changes in fluorescence across vigilance states for each interneuronal subtype. ***D***, Median changes in fluorescence of putative PYR across vigilance states (bold line). Additionally, PYR cell population was divided into sextiles according to their activity during wake (left). Histogram distribution of pyramidal cells according to their activity in REM sleep, separated into two halves, PYR with low REM activity and PYR with high REM activity (right). ***E***, Changes in fluorescence for high REM and low REM activity PYR across vigilance states. ***F***, Dynamics of calcium activity at wake onset from NREM (left), REM (middle) sleep, and at REM onset from NREM sleep (right, from −10 s to +10 s around transitions marked by a dotted gray line). Above, example raw EEG and EMG traces from the same recording session in all three conditions. Medians and median absolute deviations are represented in ***C*** and ***D***, and Friedman tests were performed. Medians are represented in ***E***, and Friedman tests were performed to compare activity during vigilance state, whereas Kruskall−Wallis tests were performed to compare activity of PYR low and high REM activity. Means and confidence intervals are represented in ***F***, and Wilcoxon signed-rank tests were performed. Further statistical details are provided in Extended Data Figure 1-1.
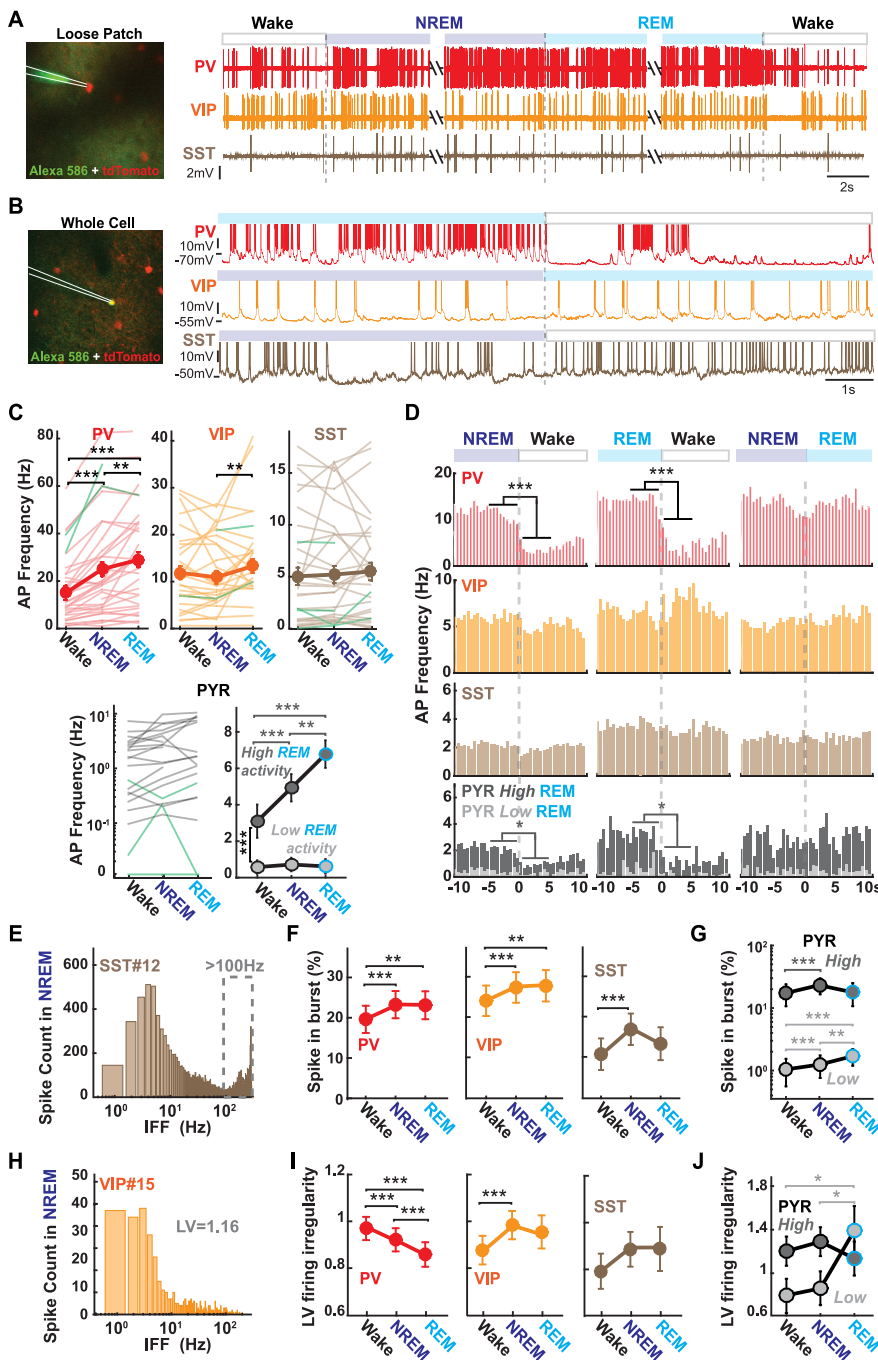
Figure 2. Sleep/wake cycle influences cortical firing rates and patterns. *A*, Loose-patch recordings. Left, A z-stack image illustrating the position of a glass pipette (white lines) in a loose-patch configuration. Right, Example raw traces for a PV, VIP, and SST neuron across different vigilance states. *B*, Whole-cell patch-clamp recordings. Left, A z-stack image illustrating the position of a glass pipette (white lines) in whole-cell-patch-clamp configuration. Right, Example membrane potential traces for a PV, VIP, and SST neuron across different vigilance states. APs have been truncated. *C*, Top, Average firing activity for each interneuronal subtype across vigilance states (bold). Individual loose-patched cells are represented in light and whole-cell patched neurons in green. Bottom left, Firing rates for putative PYR cells across vigilance states in loose-patch (gray) or whole-cell (green) configurations. Bottom right, Mean AP frequencies for high and low REM activity PYR cells. *D*, Average histograms for different vigilance state transitions (bin size = 500 ms) for each neuronal subtype. *E*, Example IFF distribution for one representative SST cell during NREM sleep. Frequency range >100 Hz was chosen to define high-frequency bursts. *F*, Percentage of high-frequency bursts according to vigilance state for PV, VIP, and SST cells. *G*, Same as in *F* but for putative PYR neurons with high and low REM activity. *H*, Same as in *E* for one representative VIP cell during NREM sleep. LV measures of the firing irregularity have been estimated for each cell and vigilance states. *I*, LV for each neuronal cell type across vigilance states. *J*, Same as in *I* but for PYR cells with high and low REM activity. Estimated means and SEMs are represented in bold in *C*, *F*, *G*, *I*, and *J*, and LMMs were performed (see above, Materials and Methods). Means are represented in *D*, and Wilcoxon signed-rank tests were performed. Information concerning mice number per transgenic line is summarized in Extended Data Figure 2-1, and a description of recording and sleep episode durations can be found in Extended Data Figure 2-2.

at wake onset but also between NREM and REM sleep in some instances. Therefore, we investigated the dynamics of AP firing rates of different neuronal cell types around those transition time points (aligned at $t = 0$ s; Fig. 2D). We quantified and compared firing rates from -5 s to 0 s and from 0 to $+5$ s. Confirming the results we found under calcium imaging a rapid decrease in PV cell firing was observed at Wake onset from either NREM or REM sleep (NREM to Wake transitions, 8.5 ± 5.2 Hz vs 1.0 ± 1.0 Hz, $n = 32$, $p < 0.001$; REM to Wake transitions, 12.7 ± 9.2 Hz vs 2.0 ± 1.2 Hz, $n = 30$, $p < 0.001$; LMM), and no changes in the firing rate of SST cells and PYR low REM activity were observed around transitions. However, we did not observe any significant change in VIP cell firing around state transitions. Finally, firing rates of PYR high REM activity cells decreased significantly as soon as the mice woke up, which was not revealed by calcium imaging data (NREM to Wake transitions, 2.3 ± 0.7 Hz vs 1.5 ± 2.3 Hz, $n = 9$, $p = 0.04$; REM to Wake transitions, 2.0 ± 3.0 Hz vs 0.0 ± 4.0 Hz, $n = 9$, $p = 0.016$; LMM).

Although cortical neurons are often classified as bursty on nonbursty on the basis of a clear bimodality in their firing interstimulus intervals (Peyrache et al., 2011), we observed that most of our recorded interneurons could fire at both high and low-frequency regimes throughout the sleep/wake cycle, as previously observed for other neuronal types, for example in the thalamus (Urbain et al., 2019). In particular, high-frequency bursts can strongly modulate synaptic integration and could therefore increase information content (Lisman, 1997). Therefore, we chose to investigate whether GABAergic and putative excitatory neuron firing patterns changed throughout the sleep/wake cycle by focusing on high-frequency bursts firing, defined as any instance of an instantaneous firing frequency (IFF) falling above 100 Hz for VIP, SST, and PYR neurons or rising above 200 Hz for PV cells (Fig. 2E). For this analysis, only episodes containing >30 spikes were taken into account. On average, the proportion of high-frequency bursts in PV and VIP neurons increased in both NREM and REM sleep compared with Wake (PV: Wake, $19.6 \pm 3.4\%$, $n = 34$; NREM, $23.2 \pm 3.4\%$, $n = 35$; REM, $23.1 \pm 3.5\%$, $n = 31$; $p < 0.001$ between Wake and NREM, $p = 0.018$ for Wake vs REM; VIP: Wake, $24.2 \pm 3.8\%$, $n = 31$; NREM, $27.5 \pm 3.8\%$, $n = 31$; REM, $27.9 \pm 3.9\%$, $n = 28$; $p < 0.001$ for Wake vs NREM, $p = 0.008$ for Wake vs REM; LMM). In contrast, SST cells, as well as

PYR neurons with high REM activity, displayed a more bursting mode specifically in NREM sleep compared with Wake (SST: Wake, 10,9% ± 3.9, $n = 29$; NREM, 17.1 ± 3.9%, $n = 30$; REM, 13.5 ± 4.1%, $n = 26$; $p < 0.001$ for Wake vs NREM; high REM PYR: Wake, 17.3 ± 6.6%; NREM, 23.2 ± 6.6%; REM, 17.9 ± 7.2%, $n = 9$; $p = 0.01$ between Wake and NREM; LMM; Fig. 2F, G). On the other hand, PYR neurons with low REM activity showed a significant increase in their bursting behavior in NREM and further more during REM sleep (low REM PYR: Wake, 1.0 ± 0.5%; NREM, 1.3 ± 0.5%; REM, 1.7 ± 0.5%, $n = 9$; $p = 0.01$ between Wake and NREM, $p < 0.001$ for Wake vs REM, $p = 0.002$ for NREM vs REM; LMM; Fig. 2G). These observed shifts in high-frequency burst firing may be related to changes in the firing irregularity of neurons. To quantify this parameter, we calculated the local coefficient of variation (LV) for which an LV of 1, >1, or <1, indicates Poisson-like, irregular and regular firing, respectively (Vinck et al., 2016; Fig. 2H). Interestingly, we found that LV firing irregularity was vigilance-state and cell-type specific. PV firing was significantly more irregular in wake, whereas VIP firing was more irregular in NREM sleep (PV: Wake, 0.97 ± 0.05, $n = 34$; NREM, 0.92 ± 0.05, $n = 35$; REM, 0.86 ± 0.052, $n = 31$; $p < 0.001$ for Wake vs NREM and Wake vs REM and NREM vs REM; VIP: Wake, 0.87 ± 0.06, $n = 31$; NREM, 0.98 ± 0.06, $n = 31$; REM, 0.95 ± 0.07, $n = 28$; $p < 0.001$ for NREM vs Wake; LMM), and SST cells displayed the same firing pattern across vigilance state (Fig. 2I). In contrast, the firing irregularity of PYR low REM activity increased significantly in REM sleep compared with Wake and NREM (low REM PYR: Wake, 0.8 ± 0.2; NREM, 0.9 ± 0.2; REM, 1.4 ± 0.2, $n = 9$; $p = 0.01$ for Wake vs REM, $p = 0.03$ for NREM vs REM; LMM), whereas the firing pattern of high REM PYR neurons remained unchanged across all vigilance states (Fig. 2J).

Timing of interneuronal firing on theta and delta oscillations

We observed a variety of oscillations on layer 2/3 LFP recorded via a glass pipette positioned nearby. LFP cortical oscillations in the theta band (5—9 Hz) have been previously observed during both wakefulness and REM sleep but not during NREM sleep (Montgomery et al., 2008; Koike et al., 2017), although the LFP electrode is usually positioned in deeper layers. Interestingly, we could also distinguish prominent theta oscillations during REM sleep on our layer 2/3 LFPs (Fig. 3C). We therefore decided to investigate phase locking of local interneurons and putative pyramidal cells to layer 2/3 LFP theta oscillations detected in Wake and REM sleep (Fig. 3A–C). First, we estimated that AP firing was significantly modulated by theta oscillations in 58% and 48% of PV cells during Wake and REM, respectively (Rayleigh's test, see above, Materials and Methods), in 60% and 43% of VIP cells, 41% and 16% of SST cells, and 47% and 44% of PYR neurons (Fig. 3D, Extended Data Fig. 3-1). Fits using von Mises' functions yielded estimates of the preferred phase (μ) and the concentration (κ) of spiking (which represents how peaked the spiking distribution is around the preferred phase; see above, Materials and Methods; Fig. 3B). Interestingly, all recorded cells fired preferentially around the trough of the theta oscillation, regardless of their neuronal identities and the vigilance state (Fig. 3E,F). On the other hand, the median concentration parameter κ of PV cells during theta oscillations observed in Wake was significantly higher than during those occurring during REM sleep ($p = 0.03$), whereas the median κ remained similar for the other cells in both Wake and REM sleep (PV κ: Wake, 0.88 ± 0.2, $n = 19$;

REM, 0.54 ± 0.15, $n = 14$, corrected Mann–Whitney test; Fig. 3E,G).

LFP delta oscillations (1–4 Hz) could be observed in all vigilance states, including REM sleep (Funk et al., 2016), although they have been shown to be mostly prominent during wakefulness (Fernandez et al., 2017) and interspersed with slow-wave activity during NREM sleep (Crunelli et al., 2006; Fig. 3H). We observed that ~70% of PV cells were modulated by delta oscillations in Wake, NREM, and REM (67, 76, and 76%, respectively). A similar proportion of VIP neurons (68, 69, and 68% for Wake, NREM, and REM, respectively) and ~40 and 55% of SST and PYR cells, respectively (SST, 39, 40, and 44%; PYR, 64%; and 50 and 56% for Wake, NREM, and REM sleep, respectively) were phase modulated by ongoing delta activity (Fig. 3I, Extended Data Fig. 3-1).

Similarly to what we observed for oscillations in the theta band, we found no difference among modulated cells of any cell type for the phase position of the peak of preferred firing on delta oscillations across all vigilance states (Fig. 3J,K). On average, median concentration median parameters κ were also unchanged for all cell types across all vigilance states (Fig. 3J,L).

Interneuronal firing activity is differentially modulated by spindles

During NREM sleep, we were able to observe clear spindle oscillations on the LFP (Fig. 4A). First, we investigated whether detected spindles (10–17 Hz, see above, Materials and Methods) during NREM sleep modulated the activity of different cortical neurons of S1 barrel layer 2/3. The firing rates of different neuronal subtypes were estimated when spindles occur (Spdl +), and when no spindles were detected on the LFP (Spdl −). On average, firing rates of both PV and PYR cells increased during spindles compared with outside spindles, whereas the AP activity of SST cells decreased during spindles (PV: Spdl −, 17.1 ± 9.9 Hz; Spdl + : 21.7 ± 12.6 Hz; $n = 35$, $p < 0.001$; PYR: Spdl −, 1.5 ± 1.3 Hz; Spdl +, 2.1 ± 2.1 Hz; $n = 22$, $p = 0.010$; SST: Spdl −, 3.2 ± 3.2 Hz; Spdl +, 2.8 ± 2.8 Hz; $n = 37$, $p = 0.0017$). In contrast, median firing rates of VIP cells remained unchanged by the occurrence of spindle (Fig. 4B).

We next investigated whether neurons could phase lock to spindles by performing a Rayleigh test, which allowed us to determine whether spiking of individual neurons was significantly locked to a particular phase of a spindle oscillation. A majority (55.9%) of PV cells were phase modulated by spindles, as 50.0% of PYR and 41.4% of VIP neurons, whereas only 18.2% of SST neurons were (Fig. 4C, Extended Data Fig. 3-1). The phase position in radians (rad) of the peak of preferred firing was significantly different for VIP cells compared with PV ($p = 0.01$) and PYR ($p = 0.003$; μ: PV, −0.05 ± 0.09 rad; VIP, 0.08 ± 0.14 rad; PYR, −0.11 ± 0.06 rad; corrected Mann–Whitney test; Fig. 4E). Indeed, VIP cells discharged 1.2 ms to 2.1 ms after PV neurons and 1.8 ms to 3.0 ms after PYR cells on spindles oscillation (for 10 and 17 Hz spindles, respectively). On the other hand, the median concentration parameter κ of PYR cells was higher than the median κ of VIP cells (PYR κ, 1.03 ± 0.4; VIP κ, 0.44 ± 0.26; $p = 0.04$; corrected Mann–Whitney test; Fig. 4F).

In some instances (~2%, range 0–18%), LFP spindles bouts were preceded by a large positive delta event (1–4 Hz), as previously observed on deeper S1-barrel cortex LFPs during NREM sleep (Urbain et al., 2019; Fig. 4A). These delta events are thought to correspond to periods of cortical quiescence (Contreras and Steriade, 1995; Maingret et al., 2016). We quantified normalized firing rates before,
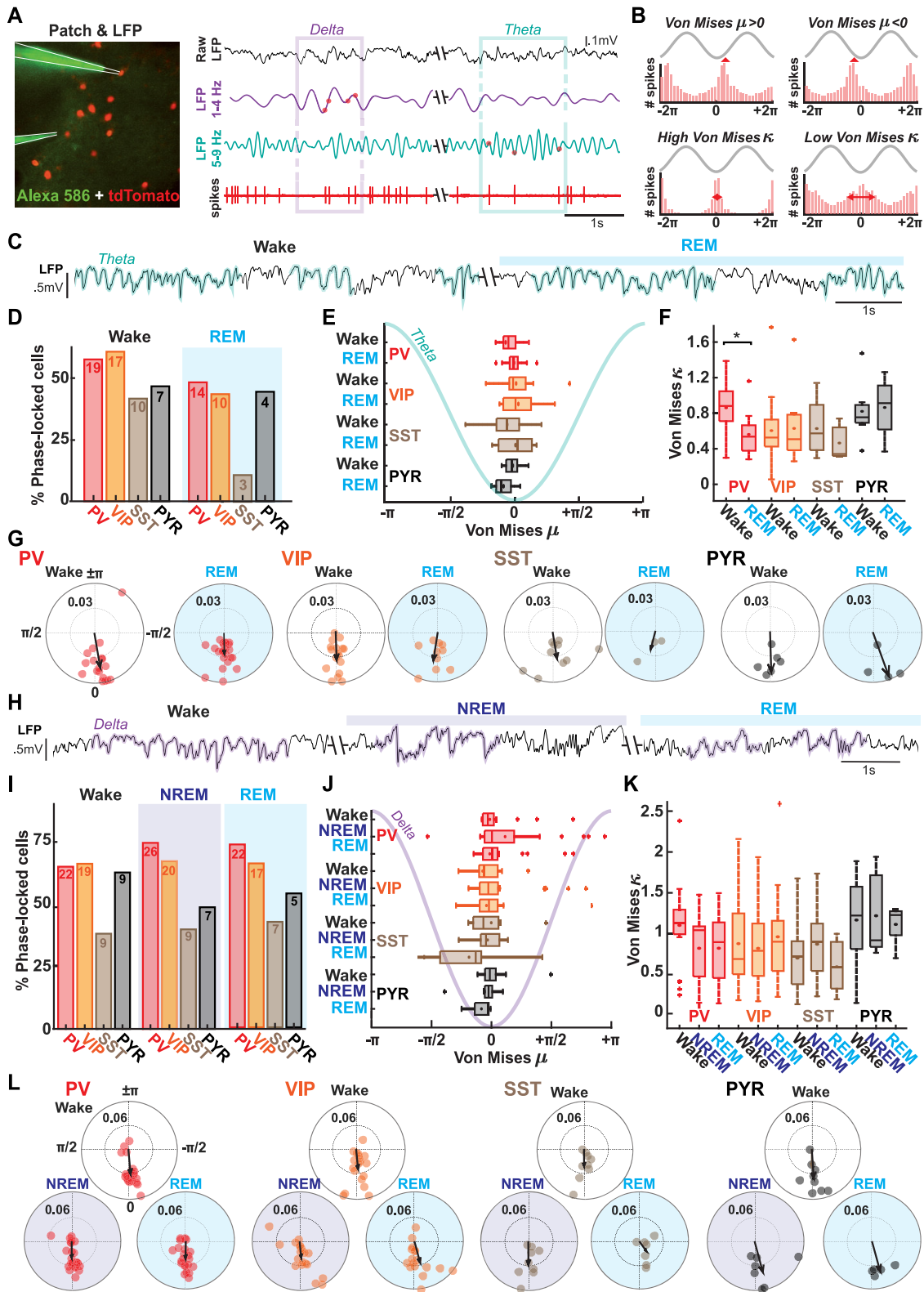
Figure 3. Theta and delta oscillations phase locking of spikes across vigilance states. *A*, Spike timing on delta (1–4 Hz) and theta (5–9 Hz) bouts detected on filtered wS1 LFP (see above, Materials and Methods). *B*, Two parameters extracted per cell; the peak μ (top) and the concentration κ (bottom) of the phase locking computed from a Von Mises curve fitting on spike distribution. *C*, Example raw LFP trace showing detected theta bouts (green) during wake (left) and REM sleep (right). *D*, Percentage of neurons phased locked to theta oscillations in wake and REM. A Rayleigh test was performed on each cell to detect if they were modulated by theta oscillations (*p* < 0.01). *E*, Average peaks of the phase locking by neuronal subtype. *F*, Average concentration of the phase locking by neuronal subtype. *G*, Circular plots for all neurons modulated by theta oscillations in wake and in REM. Each dot represents a modulated cell, and the arrows represent the mean for that population. *H*, Example raw LFP trace showing detected delta bouts (violet) during wake (left), NREM (middle), and REM sleep (right). *I*, Same as in *D* for delta oscillations detected in wake, NREM, and REM sleep. *J*, Same as in *E* for delta oscillations. *K*, Same as in *F* for delta oscillations. *L*, Same as in *G* for delta oscillations occurring in wake, NREM, and REM sleep. The 25th and 75th percentiles are represented with median (bar) and mean (dot) in box plots in *F*, *G*, *K*, and *L*; Kruskal–Wallis tests were performed. A summary of animals and modulated cell numbers per oscillation type is provided in Extended Data Figure 3-1.
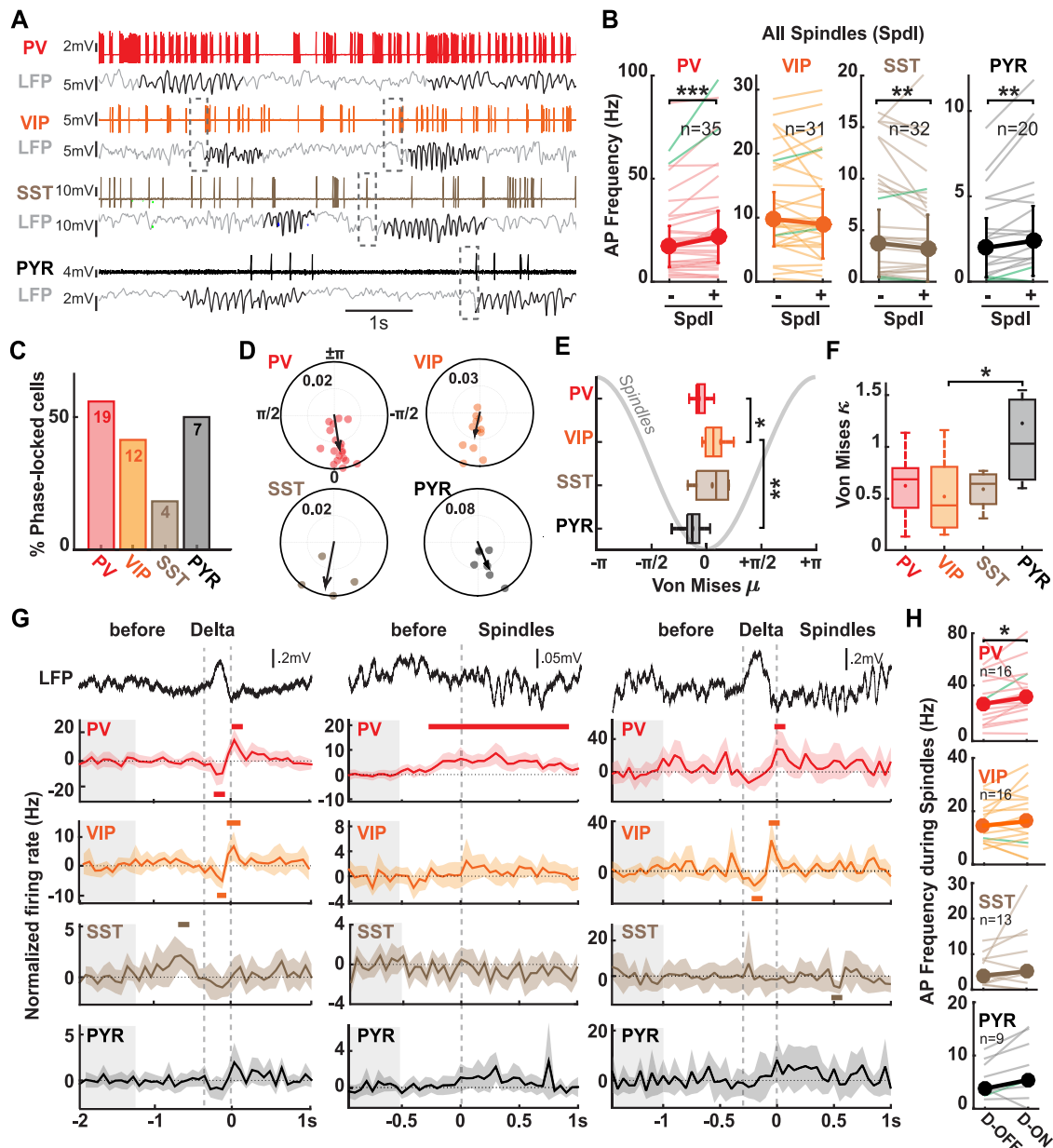
Figure 4. Modulation of interneuronal firing rates by sleep spindles in NREM sleep. ***A***, Example raw traces from a PV (top), VIP, SST, and PYR (bottom) neuron together with ongoing LFP activity. Spindle bouts are denoted in black. Delta events occurring before spindle bouts are indicated by dashed gray boxes. ***B***, Average AP frequency (bold lines) during spindles (Spdl +) and outside spindles (Spdl −) for each cell type. Cells recorded in whole-cell patch mode are shown in green. ***C***, Percentage of neurons phased locked to spindle oscillations. A Rayleigh test was performed on each cell to detect if the cells were modulated by sleep spindles ($p < 0.01$). ***D***, Circular plots for all modulated cells. Each circle represents a modulated cell, and the vector represents the mean for all modulated neurons. ***E***, Average peaks of the phase locking by neuronal subtype. ***F***, Average concentrations of the phase locking by neuronal subtype. ***G***, Average firing rates across delta event (D-event; left), spindles (middle), and D-event spindles (right) for each cell type. Traces were baselined during the first 500 ms. ***H***, Median firing rates during entire spindle depending on the absence (D-OFF) or the presence (D-ON) of delta event before. Medians and median absolute deviations are represented in *B* and *H*. Wilcoxon signed-rank tests were performed in *B* and *H*. The 25th and 75th percentiles are represented with median (bar) and mean (dot) in box plots in *E* and *F*; Kruskal–Wallis tests were performed. Means and confidence intervals are represented in *G*.

during delta events when they occurred (D-event), and during spindles (Spdl) and examined how the presence or absence of such delta events influenced their dynamics. On average, all neuron subtypes tend to display increased firing rates during spindles compared with delta events, but results reach significance only for PV and VIP cells (PV: before, 15.0 ± 7.2 Hz; D-event, 7.5 ± 7.5 Hz; Spdl, 28.3 ± 16.5 Hz; $n = 14$; $p = 0.04$ between before and D-event, $p < 0.001$ between D-event and Spdl; VIP: before, 9.0 ± 5.5 Hz; D-event, 10.0 ± 5.0 Hz; Spdl, 17.6 ± 6.7 Hz; $n = 12$; $p = 0.01$ between before and Spdl, $p = 0.02$ between D-event and

Spdl; Fig. 4*H*). Interestingly, the overtime analysis showed us that the increase activity of VIP cells specifically appears at the end of the delta event (Fig. 4*G*).

We then wondered whether the neuronal activity could differ during a spindle, depending on whether it was preceded by a delta event. Results showed that all neuronal cell types, except SST cells, displayed a stronger firing rate during spindles preceded by a delta event (PV: Spdl, 13.1 ± 5.0 Hz; D-event–Spdl, 28.3 ± 16.5 Hz; $n = 14$, $p = 0.013$; VIP: Spdl, 10.8 ± 5.1 Hz; D-event–Spdl, 17.6 ± 6.7 Hz; $n = 12$, $p < 0.001$; PYR: Spdl, 0.9 ± 0.9 Hz; D-event–Spdl, 3.8 ± 3.8 Hz; $n = 9$, $p = 0.03$; Fig. 4*I*).
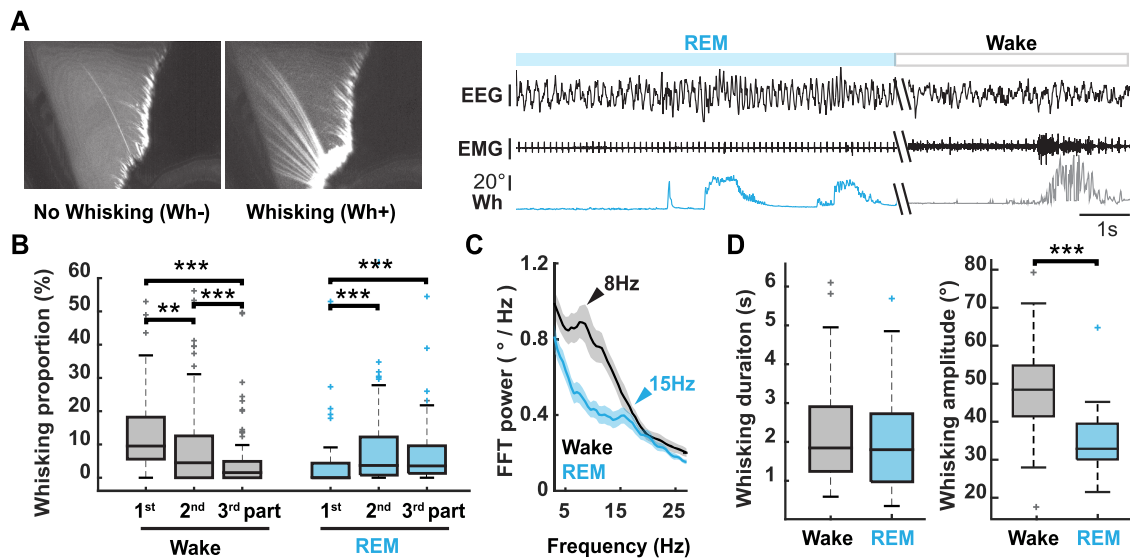
Figure 5. Whisking bouts occur during both wake and REM sleep in naturally sleeping mice. *A*, Left, Mean picture of C2 whisker observed through a high-speed infrared camera in the absence or presence of whisker protractions. Right, Example EEG (top), EMG (middle), and Whisker position (bottom) traces during REM sleep and wake, showing bouts of whisking (>1 s) in both vigilance states. Scale bars: EEG, 0.2; EMG, 0.1 mV. *B*, Percentage of time spent whisking during the first, second, and third part of wake and REM sleep across all recorded episodes. Dots denote results per recording session. *C*, Grand mean average FFT of whisker position during whisking bouts occurring in wake (black) and REM sleep (cyan). FFTs were computed from 1 s time windows for all bouts across all recording sessions. A peak at ~8 Hz during wake whisking and at 15 Hz during REM whisking are marked by black and blue arrows respectively. *D*, Average whisking bout durations (left) and amplitudes (right) during wake and REM sleep. The 25th and 75th percentiles are represented with median (bar) in box plots in *B* and *D*. Friedman tests were performed in *B*, and Wilcoxon signed-rank tests were performed in *D*. Means and confidence intervals are represented in *C*.

Whisking episodes can occur during REM sleep

One of the most striking behavioral features of rodents, which they mainly display during exploration of their environment, is their ability to actively sweep their whiskers back and forth (Welker, 1964). Interestingly, we observed long-lasting (>1 s) C2 whisker movements during both active wakefulness and throughout the time course of REM sleep episodes (Fig. 5A). Those bouts were not equally distributed over the time course of a wake nor REM episode, occurring over longer periods of time at the start of a Wake episode and toward the end of an REM episode, respectively (Wake: percentage of time spent whisking, first part, $9.8 \pm 8.3\%$; second part, $4.5 \pm 8.7\%$; third part, $1.5 \pm 5.4\%$; $n = 92$; $p = 0{,}003$ for first vs second part, $p < 0.001$ for first vs third part, $p < 0.001$ for second vs third part; REM: percentage of time spent whisking, first part, $0.0 \pm 4.6\%$; second part, $3.6 \pm 8.8\%$; third part, $6.2 \pm 3.6\%$; $n = 70$; $p < 0.001$ for first vs both second and third parts; Fig. 5B). Whisking bouts in REM further differed from their wake counterparts in their frequency of protraction/retraction oscillations, with faster but smaller amplitude series of sweeps superimposed over an already large baseline deflection angle of the C2 whisker occurring during REM sleep (peak at ~8 Hz for whisking bouts occurring during wake vs a peak at ~15 Hz for whisking bouts occurring during REM sleep, Fig. 5A,C), and their median maximal amplitudes (Wake, $46.2 \pm 8.1°$, $n = 92$; REM, $32.8 \pm 5.5°$, $n = 70$; $p < 0.001$; Fig. 5D). However, their durations were similar to those occurring during wake (Whisking bouts duration: Wake, 1.85 ± 0.97 s, $n = 92$; REM, 1.76 ± 1.76 s, $n = 70$; Fig. 5D). Mice therefore display whisking bouts with specific characteristics during REM sleep, but their durations preclude them from being categorized as twitches (Tiriac et al., 2012).

Whisking induces changes in interneuronal firing activity during both wake and REM sleep

Previous studies uncovered differential modulations of GABAergic cell neuronal firing during free whisking (Gentet et al., 2010, 2012;

Muñoz et al., 2017) or active tactile behavior (Yu et al., 2019). As we observed whisking behavior in our head-restrained, naturally sleeping mice, during both wake and REM sleep, we next examined whether it could differentially affect neuronal firing rates in our population of layer 2/3 cortical neurons during these two fundamentally different cognitive brain states (Fig. 6). We quantified the average firing rates of different cellular subtypes when the mouse was whisking (Wh+) versus when no whisking occurred (Wh−). Furthermore, twitches were excluded from the analysis (see above, Materials and Methods). We observed different patterns of activity across different cells in both loose-patch (Fig. 6A) and whole-cell patch-clamp (Fig. 6B) configurations. On population data, AP firing in both PV and PYR neurons was not modulated by whisking bouts occurring during either wake nor REM sleep. On the other hand, VIP cell firing activity was increased during whisking in both wake and REM sleep (Wake Wh−, 9.4 ± 6.1 Hz; Wake Wh+, 19.0 ± 9.9 Hz; $n = 28$; REM Wh−, 10.7 ± 5.4 Hz; REM Wh+, 13.4 ± 6.3 Hz; $n = 23$; $p < 0.001$ for whisking effects in Wake, $p = 0.01$ for whisking effects in REM). In contrast, SST cell firing significantly decreased on whisking in wake (Wake Wh−, 4.0 ± 3.2 Hz; Wake Wh+, 3.2 ± 3.0 Hz; $n = 27$, $p = 0.02$) and also tended to decrease during whisking bouts in REM sleep (REM Wh−, 6.3 ± 5.4 Hz; REM Wh+, 4.9 ± 4.9 Hz; $n = 15$; Fig. 6C). These results on population averages may not, however, reflect the behavior of individual neurons during whisking throughout the sleep/wake cycle. Therefore, to better understand whether whisking could differentially affect the firing rates of different neurons, we subtracted individual neuronal firing rates during whisking by the firing rates during nonwhisking, divided by the firing rate during nonwhisking to obtain an index as a percentage change for each cell. We defined cells as Whisk-activated or Whisk-inactivated when that index exceeded +15 and −15%, respectively. Over half of PV cells were classified as Whisk activated during whisking in wakefulness (53%), whereas 29% was classified as Whisk inactivated. During REM sleep, however, PV neuron activity remained
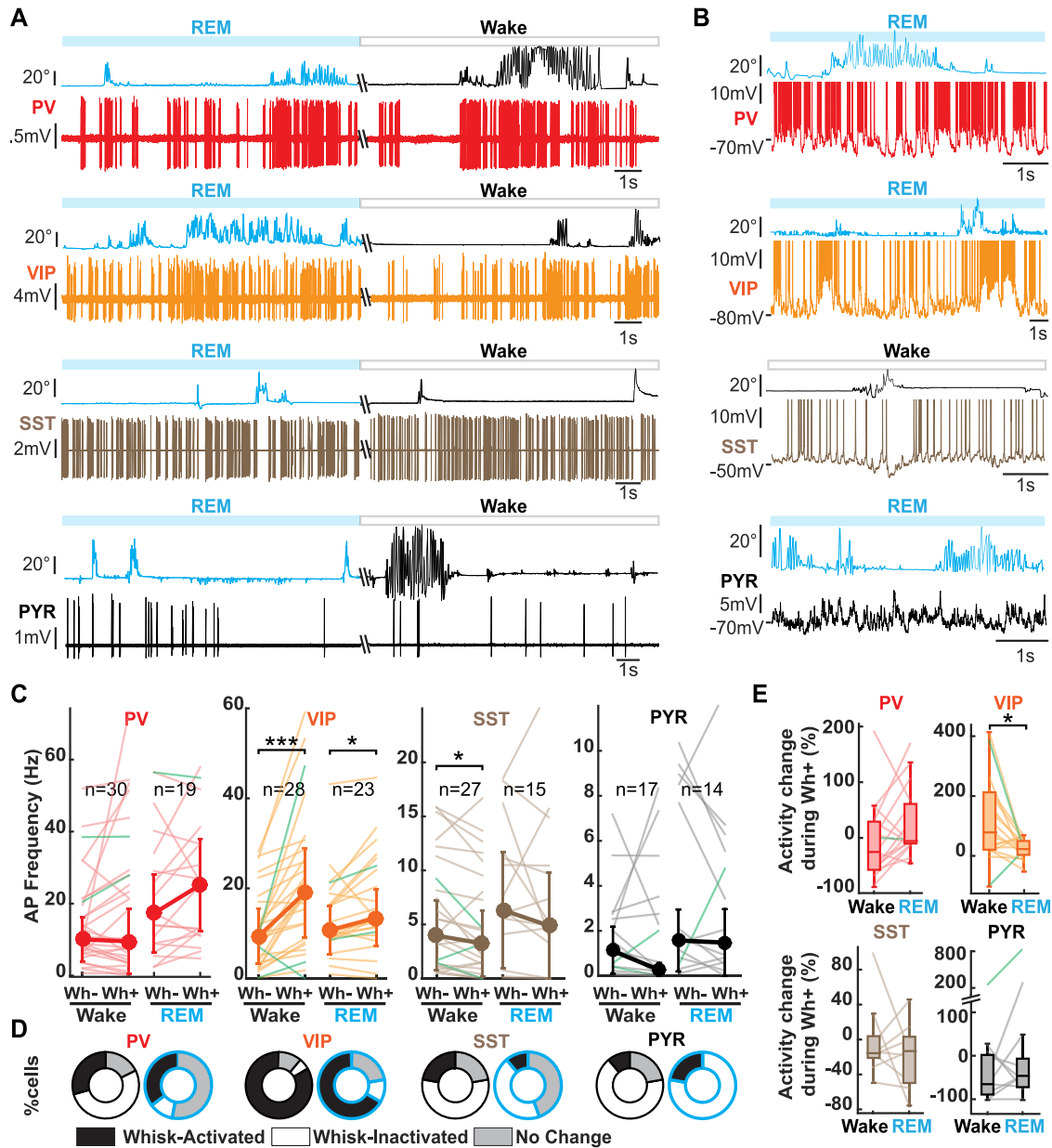
Figure 6. Whisking modulates cortical interneurons firing rates. **A**, Example raw traces of loose-patch recordings and whisker movements in wake and REM sleep for one PV (red), one VIP (orange), one SST (beige), and one PYR (black). **B**, Example raw traces of whole-cell recordings and whisker movement in wake or REM sleep (same color code as in **A**). **C**, Median firing rates for PV, VIP, SST, and PYR neurons during whisking bouts (Wh+) versus no whisking (Wh−). Cells recorded in loose patch are represented in light color and whole-cell patch-clamped neurons in green. **D**, Percentage of cells per subtype and per vigilance state displaying either increased, decreased, or no change in their firing rates during Wh+ versus Wh−. **E**, Firing activity change in percentage during whisking in wake sleep versus REM compared with no whisking in wake and REM sleep. Medians and median absolute deviations are represented in **C**. The 25th and 75th percentiles are represented with median (bar) in box plots in **E**. Wilcoxon signed-rank test were performed in **C** and **E**.

unchanged in a majority of cells (53%). In contrast, during both wake and REM sleep, a large proportion of VIP cells qualified as Whisk activated (83 and 67%, respectively), whereas only a small proportion was classified as Whisk inactivated (11 and 22%, respectively; Fig; 6D). On the other hand, most of our recorded SST and PYR neurons were categorized as Whisk inactivated (SST, 56 and 44%; PYR, 67 and 78% for wake and REM sleep, respectively; Fig; 6D). Finally, we compared the percentage changes in wake and REM for each neuron grouped by subtype to examine whether individual neuronal firing rates could be differentially modulated by whisking in wake versus REM sleep. In our population of VIP cells, this percentage change dropped significantly in REM compared with wake, indicating that the increase in VIP cell AP firing that occurs during whisking in

wake is larger than the increase observed during REM sleep (VIP Wake percentage change during whisking, +78.5 ± 69.4% vs +22.7 ± 23.6% in REM; n = 18, p = 0.01). For PV, PYR, and SST neurons, the observed firing rate changes during whisking remained stable on average in Wake compared with REM sleep (Fig. 6E). In summary, we observed a stronger homogeneity among our population of VIP cells, whereas PV, SST, and PYR neurons displayed more heterogeneous patterns of firing activity on whisking.

Discussion

Cortical activity throughout the sleep/wake cycle needs to be highly dynamic to perform different behavioral tasks during
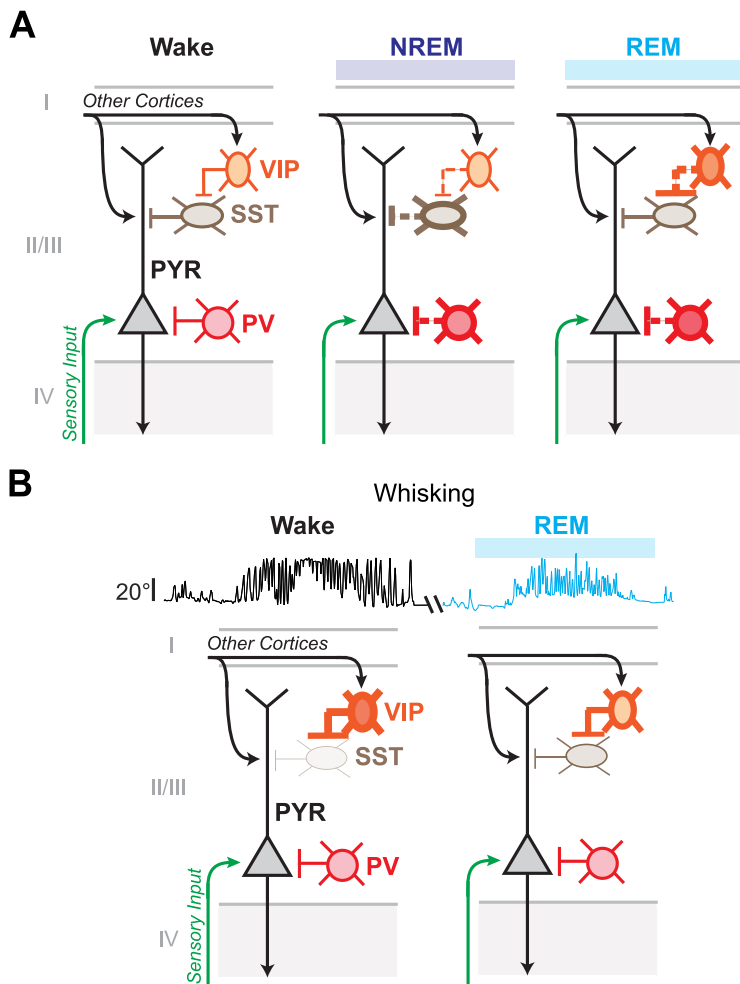
Figure 7. Simplified circuit diagram of layer 2/3 of S1 cortex during the three main vigilance states. **A**, During NREM sleep, PV activity increases, weakening the impact of sensory inputs at the level of the soma of principal neurons (PYR). Increased SST bursting activity partially disrupts corticocortical communication at the level of the distal parts of PYR cells. During REM sleep, strong activation of VIP neurons leads to SST disinhibition, allowing for the re-establishment of corticocortical information integration. **B**, During whisking in both wake and, to a lesser extent, REM sleep, increase of VIP activity further opens up the corticocortical stream while maintaining the integration levels of sensory inputs.

transgenic mouse lines where genetically identified subpopulations of GABAergic neurons could be visualized. This initial study first revealed that PV cell activity is increased during both NREM and REM sleep stages, VIP activity is increased specifically during REM sleep, and SST and PYR neuronal activity remains overall stable over the time course of the sleep/wake cycle. These findings share both similarities and differences with a previous study in the motor cortex, showing elevated PV cell activity during REM but reduced activity of PV, SST, and PYR neurons during NREM compared with wakefulness (Niethard et al., 2016). Such discrepancies could be explained by differences in the brain region under investigation, experimental procedures, or scoring methodology. The fact that we used extended habituation sessions compared with previous studies might have both led to reduced animal stress levels and an attenuation of new information encoding. In addition, our recordings were scored manually with a temporal precision of 100 ms, whereas Niethard et al. (2016) used an automatic scoring approach that categorized vigilance states in series of 10 s epochs. Thus, the scoring method that we used, for example, enabled us to identify short arousal segments occurring within an NREM sleep episode and score them accordingly (Urbain et al., 2019). Finally, most of the calcium recordings were manually started once the animal entered NREM sleep to prevent bleaching and to ensure that all three main vigilance states could be recorded. This method could have potentially increased the proportion of quiet wakefulness in our data compared with other studies. In any case, our results under calcium imaging were confirmed by our targeted recordings of individual neurons in loose-patch or whole-cell patch-clamp configurations. Such recordings also offer the advantage of a more precise temporal resolution of AP firing than calcium imaging and allowed us to simultaneously record the LFP by placing a glass pipette within layer 2/3 of the same column from which our targeted single-unit recordings originated (Perrenoud et al., 2016). Using this combination of recording elements, we first confirmed our findings that overall activity of PV cells is significantly increased in both NREM and REM sleep compared with wake and that VIP cells are specifically more active during REM sleep (Fig. 7A). These measures of cell type-specific average firing activity according to vigilance states offer a good indicator that the excitatory/inhibitory balance is highly dynamic across the sleep/wake cycle. In our study, we further investigated those dynamics along transitions between vigilance states, and we found that PV activity rapidly decreased at wake onset from NREM and REM sleep episodes, as previously reported for transitions from NREM to wake for fast-spiking, putative PV neurons in the mouse frontal cortex (Miyawaki et al., 2019). This rapid decrease could be because of the rapid activation of the ascending arousal system. For example, wake-specific histaminergic neurons of the tuberomamillary nucleus and norepinephrine neurons of the locus ceruleus, both with extensive projections throughout the cerebral cortex, have been shown to rapidly activate at wake onset (Takahashi et al., 2006).

wakefulness and allow the consolidation or removal of unnecessary memory traces during sleep (Kay and Frank, 2019). Local GABAergic interneurons can efficiently control the spike timing of principal neurons via their precise targeting of different regions of the somatodendritic arborizations of pyramidal cells (Gentet, 2012). Layer 2/3 of the somatosensory barrel (wS1) cortex is involved in the processing of whisker sensory information and can perform computations of both simple and complex tasks in a goal-oriented manner (Petersen, 2019). Although PV cells primarily exert perisomatic inhibition onto excitatory cells (Kawaguchi and Kubota, 1997), SST cells, composed essentially of Martinotti-type neurons (Jiang et al., 2015), control the dendritic encoding of synaptic inputs in the somatosensory cortex (Murayama and Larkum, 2009; Gentet et al., 2012; Fig. 7A). How local GABAergic inhibitory cells regulate this circuit during different vigilance states of the sleep/wake cycle and how ongoing brain oscillations or whisking behaviors modulate their firing patterns or activity remain, however, poorly understood.

In this study, we first performed calcium imaging of neuronal population activity in layer 2/3 of wS1 in different

Notably, we found that distribution of pyramidal cell activity broadened during REM sleep as described by Miyawaki et al. (2019). We therefore decided to the split pyramidal cell population into two subgroups on the basis of their basal activity during REM. Although activity at the population level remained stable across vigilance states, this separation uncovered subtler changes in the activity of principal neurons throughout the sleep/wake cycle. The neurons with the highest basal levels of REM activity were significantly less active during wake and NREM sleep, whereas neurons with low REM activity did not display any significant overall changes in AP firing frequency across vigilance states, indicating that specific cortical circuits may be upregulated during REM sleep. Indeed, a recent study by Niethard et al. (2021) found that separating pyramidal neurons into two groups based on the level of change in their firing activity during sleep spindles uncovered a substrate for upregulation of specific circuits possibly implicated in memory consolidation. Although increased neuronal activity of PV cells during NREM sleep would be expected to contribute to synaptic downscaling, we did not observe a concomitant overall decrease in principal cell firing, suggesting that at the level of pyramidal neurons of the local S1 layer 2/3 circuit, more complex, compartment-specific synaptic modulation might take place during sleep.

Indeed, although the average AP activity of SST neurons remained stable across the sleep/wake cycle, their firing patterns, as well as those of other types of interneurons, shifted to a more burst-like behavior during NREM sleep compared with wake. This shift could be explained by the more synchronized state of cortex during NREM sleep, with the time windows for neuronal firing being temporally restricted for all neurons compared with wake (Fig. 7A). However, the firing irregularity of GABAergic neurons was differentially modulated during NREM sleep, with increased firing irregularity being present in VIP neurons but not PV nor SST cells. Thus, VIP neurons may play a major role in the reorganization of GABAergic neuronal activity patterns during NREM through its strong disinhibitory influence over local cortical interneurons (Pfeffer et al., 2013). The important role of VIP neuron firing dynamics during NREM was further evidenced by their firing behavior during sequences of delta event spindles. Delta events preceding spindles have recently been shown to play a role in memory consolidation via the recruitment of local cell assemblies performing isolated cortical computations (Todorova and Zugaro, 2019). Interestingly, we observed subtle temporal changes in the activity of GABAergic VIP neurons over the time course of LFP delta–spindles sequences, which suggests that the disinhibitory control exerted by this interneuronal subpopulation is reduced during delta events but rises quickly toward the end and at the time of emergence of spindle oscillations (Fig. 4G). This could lead to short, but temporally precise, time windows during which removal of inhibition onto excitatory cell assemblies would allow cortical replay sequences to be conducted (Ji and Wilson, 2007).

During NREM sleep, we further found an increased activity during periods of LFP spindles in both PV and excitatory layer 2/3 pyramidal neuron populations but a decrease in SST overall neuronal activity, as previously reported across different cortical regions (Niethard et al., 2018). In addition, we report than among neurons that were modulated by spindle oscillations, PV and pyramidal cells fired at a preferentially earlier phase than their VIP counterparts, indicating that these cells might contribute to the emergence and/or amplification of these LFP oscillations through their sequential activation. Although spindles are considered to be thalamic in origin and induce phase locking of rhythms in both neocortical and hippocampal networks (Latchoumane et al., 2017), it is currently unclear whether the spindles that we recorded on our LFP electrodes are mainly a representation of these propagating spindles, an emanation of local circuit properties, or a combination of both as LFPs are notoriously difficult to interpret (Einevoll et al., 2013).

A majority of local cortical neurons were modulated by ongoing LFP slow delta oscillations during both wake and sleep. Only SST neurons displayed relatively weaker modulation, in accordance with a previous finding suggesting that their membrane potential dynamics were not correlated to those of surrounding neurons during quiet wakefulness (Gentet et al., 2012). Interestingly, this weaker modulation remained stable throughout the sleep/wake cycle as well as the preferred phase locking of all cortical neurons.

Whisking behavior in rodents is associated with their nocturnal foraging habits as they explore their environment through the whisker sensing of surrounding objects (Petersen, 2014). Although during REM sleep, mice display, just like humans, rapid-eye movements (Fulda et al., 2011), we surprisingly observed long-lasting bouts of whisking behavior in mice during REM sleep, despite the complete body muscle atonia. We distinguish these bouts of whisking from previously reported REM twitches in the rat neonate (Tiriac et al., 2012) by their durations (over 1 s vs a few tens of milliseconds for twitches) and the amplitude of their protraction. Nevertheless, they differed from their wake counterparts in their higher peak frequency of oscillations, corresponding to smaller but faster protraction/retraction sweeps from an already protracted whisker position from rest. In this article, we first confirm results obtained from previous studies showing whisking-related changes in interneuronal AP firing in awake head-fixed mice, Although PV cells displayed heterogeneous modulation of their activity following the onset of free whisking, VIP neurons were more consistently activated during whisking, whereas SST firing was reduced, as in previous findings (Gentet et al., 2010, 2012; Lee et al., 2013; Muñoz et al., 2017). During REM sleep, however, whisking induced smaller increases and no significant decrease in VIP and SST neuronal activity, respectively (Fig. 7B). This differential modulation of VIP neurons and their target SST cells could help isolate the local circuit from top-down corticocortical and thalamic afferents impinging onto distal dendrites of excitatory principal pyramidal cells (Oda et al., 2004; Larkum et al., 2009). This raises the interesting prospect that REM whisking bouts might correspond to a brain state during which internalization of awake whisking behavior is re-experienced.

In summary, our study sheds light on the complex interplay between local cortical interneuronal firing activity and ongoing brain oscillatory dynamics across different vigilance states. Especially, we have shown that PV and VIP neurons may play prominent roles in dynamically suppressing, disengaging, or activating the local circuits at important time points of the sleep/wake cycle. The functional consequences of this dynamic interplay might be better observed at the level of perception of sensory inputs during sleep (Velluti, 1997; Nir et al., 2015) or consolidation of sensory memory traces acquired during wake (Buzsáki, 1989; van Dongen et al., 2011).

References

Atallah BV, Bruns W, Carandini M, Scanziani M (2012) Parvalbumin-expressing interneurons linearly transform cortical responses to visual stimuli. Neuron 73:159–170.

Bates D, Mächler M, Bolker BM, Walker SC (2015) Fitting linear mixed-effects models using lme4. J Stat Softw 67:1–48.

Berens P (2009) CircStat: A MATLAB toolbox for circular statistics. J Stat Softw 31:1–21.

Born J, Rasch B, Gais S (2006) Sleep to remember. Neuroscientist 12:410–424.

Bouchard MB, Chen BR, Burgess SA, Hillman EMC (2009) Ultra-fast multi-spectral optical imaging of cortical oxygenation, blood flow, and intracellular calcium dynamics. J Neuropathol Exp Neurol 17:509–509.

Buzsáki G (1989) Two-stage model of memory trace formation: a role for "noisy" brain states. Neuroscience 31:551–570.

Buzsáki G (2002) Theta oscillations in the hippocampus. Neuron 33:325–340.

Chen TW, Wardill TJ, Sun Y, Pulver SR, Renninger SL, Baohan A, Schreiter ER, Kerr RA, Orger MB, Jayaraman V, Looger LL, Svoboda K, Kim DS (2013) Ultrasensitive fluorescent proteins for imaging neuronal activity. Nature 499:295–300.

Cirelli C (2017) Sleep, synaptic homeostasis and neuronal firing rates. Curr Opin Neurobiol 44:72–79.

Contreras D, Steriade M (1995) Cellular basis of EEG slow rhythms: a study of dynamic corticothalamic relationships. J Neurosci 15:604–622.

Crunelli V, Cope DW, Hughes SW (2006) Thalamic T-type Ca 2+ channels and NREM sleep. Cell Calcium 40:175–190.

Einevoll GT, Kayser C, Logothetis NK, Panzeri S (2013) Modelling and analysis of local field potentials for studying the function of cortical circuits. Nat Rev Neurosci 14:770–785.

Fang G, Zhang C, Xia Y, Lai Y, Liu T, You Z, Yao D (2009) The effect of different EEG derivations on sleep staging in rats: the frontal midline-parietal bipolar electrode for sleep scoring. Physiol Meas 30:589–601.

Fernandez LMJ, Comte JC, Le Merre P, Lin JS, Salin PA, Crochet S (2017) Highly dynamic spatiotemporal organization of low-frequency activities during behavioral states in the mouse cerebral cortex. Cereb Cortex 27:5444–5462.

Frankland PW, Bontempi B (2005) The organization of recent and remote memories. Nat Rev Neurosci 6:119–130.

Fulda S, Romanowski CPN, Becker A, Wetter TC, Kimura M, Fenzel T (2011) Rapid eye movements during sleep in mice: high trait-like stability qualifies rapid eye movement density for characterization of phenotypic variation in sleep patterns of rodents. BMC Neurosci 12:110.

Funk CM, Honjoh S, Rodriguez AV, Cirelli C, Tononi G (2016) Local slow waves in superficial layers of primary cortical areas during REM sleep. Curr Biol 26:396–403.

Funk CM, Peelman K, Bellesi M, Marshall W, Cirelli C, Tononi G (2017) Role of somatostatin-positive cortical interneurons in the generation of sleep slow waves. J Neurosci 37:9132–9148.

Gasselin C, Hohl B, Vernet A, Crochet S, Staiger JF, Petersen CCH (2021) Cell-type specific nicotinic input disinhibits mouse barrel cortex during active sensing. Neuron 109:778–787.

Gentet LJ (2012) Functional diversity of supragranular GABAergic neurons in the barrel cortex. Front Neural Circuits 6:52.

Gentet LJ, Avermann M, Matyas F, Staiger JF, Petersen CCH (2010) Membrane potential dynamics of GABAergic neurons in the barrel cortex of behaving mice. Neuron 65:422–435.

Gentet LJ, Kremer Y, Taniguchi H, Huang ZJ, Petersen CCH (2012) Unique functional properties of somatostatin-expressing GABAergic neurons in mouse barrel cortex. Nat Neurosci 15:607–612.

Girardeau G, Benchenane K, Wiener SI, Buzsáki G, Zugaro MB (2009) Selective suppression of hippocampal ripples impairs spatial memory. Nat Neurosci 12:1222–1223.

Goldey GJ, Roumis DK, Glickfeld LL, Kerlin AM, Reid RC, Bonin V, Schafer DP, Andermann ML (2014) Removable cranial window for long-term imaging in awake mice. Nat Protoc 9:2515–2538.

Goltstein PM, Coffey EB, Roelfsema PR, Pennartz CM (2013) In vivo two-photon Ca2+ imaging reveals selective reward effects on stimulus-specific assemblies in mouse visual cortex. J Neurosci 33:11540–11555.

Hobson JA, McCarley RW (1971) Cortical unit activity in sleep and waking. Electroencephalogr Clin Neurophysiol 30:97–112.

Ji D, Wilson MA (2007) Coordinated memory replay in the visual cortex and hippocampus during sleep. Nat Neurosci 10:100–107.

Jiang X, Shen S, Cadwell CR, Berens P, Sinz F, Ecker AS, Patel S, Tolias AS (2015) Principles of connectivity among morphologically defined cell types in adult neocortex. Science 350:aac9462.

Kawaguchi Y, Kubota Y (1997) GABAergic cell subtypes and their synaptic connections in rat frontal cortex. Cereb Cortex 7:476–486.

Kay K, Frank LM (2019) Three brain states in the hippocampus and cortex. Hippocampus 29:184–238.

Klinzing JG, Niethard N, Born J (2019) Mechanisms of systems memory consolidation during sleep. Nat Neurosci 22:1598–1610.

Koike BDV, Farias KS, Billwiller F, Almeida-Filho D, Libourel PA, Tiran-Cappello A, Parmentier R, Blanco W, Ribeiro S, Luppi PH, Queiroz CM (2017) Electrophysiological evidence that the retrosplenial cortex displays a strong and specific activation phased with hippocampal theta during paradoxical (REM) sleep. J Neurosci 37:8003–8013.

Larkum ME, Nevian T, Sandler M, Polsky A, Schiller J (2009) Synaptic integration in tuft dendrites of layer 5 pyramidal neurons: a new unifying principle. Science 325: 756–760.

Latchoumane CFV, Ngo HVV, Born J, Shin HS (2017) Thalamic spindles promote memory formation during sleep through triple phase-locking of cortical, thalamic, and hippocampal rhythms. Neuron 95:424–435.e6.

Lee S, Kruglikov I, Huang ZJ, Fishell G, Rudy B (2013) A disinhibitory circuit mediates motor integration in the somatosensory cortex. Nat Neurosci 16:1662–1670.

Lisman JE (1997) Bursts as a unit of neural information: making unreliable synapses reliable. Trends Neurosci 20:38–43.

Maingret N, Girardeau G, Todorova R, Goutierre M, Zugaro M (2016) Hippocampo-cortical coupling mediates memory consolidation during sleep. Nat Neurosci 19:959–964.

Margrie TW, Meyer AH, Caputi A, Monyer H, Hasan MT, Schaefer AT, Denk W, Brecht M (2003) Targeted whole-cell recordings in the mammalian brain in vivo. Neuron 39:911–918.

Markram H, Toledo-Rodriguez M, Wang Y, Gupta A, Silberberg G, Wu C (2004) Interneurons of the neocortical inhibitory system. Nat Rev Neurosci 5:793–807.

Miyawaki H, Watson BO, Diba K (2019) Neuronal firing rates diverge during REM and homogenize during non-REM. Sci Rep 9: 689.

Montgomery SM, Sirota A, Buzsáki G (2008) Theta and gamma coordination of hippocampal networks during waking and rapid eye movement sleep. J Neurosci 28:6731–6741.

Muñoz W, Tremblay R, Levenstein D, Rudy B (2017) Layer-specific modulation of neocortical dendritic inhibition during active wakefulness. Science 355:954–959.

Murayama M, Larkum ME (2009) Enhanced dendritic activity in awake rats. Proc Natl Acad Sci U S A 106:20482–20486.

Niethard N, Hasegawa M, Itokazu T, Oyanedel CN, Born J, Sato TR (2016) Sleep-stage-specific regulation of cortical excitation and inhibition. Curr Biol 26:2739–2749.

Niethard N, Ngo H-VV, Ehrlich I, Born J, Hertie D (2018) Cortical circuit activity underlying sleep slow oscillations and spindles. Proc Natl Acad Sci USA 115:E9220–E9229.

Niethard N, Brodt S, Born J (2021) Cell-type specific dynamics of calcium activity in cortical circuits over the course of slow-wave sleep and rapid eye movement sleep. J Neurosci 41:4212–4222.

Nir Y, Vyazovskiy VV, Cirelli C, Banks MI, Tononi G (2015) Auditory responses and stimulus-specific adaptation in rat auditory cortex are preserved across NREM and REM sleep. Cereb Cortex 25:1362–1378.

Oda S, Kishi K, Yang J, Chen S, Yokofujita J, Igarashi H, Tanihata S, Kuroda M (2004) Thalamocortical projection from the ventral posteromedial nucleus sends its collaterals to layer I of the primary somatosensory cortex in rat. Neurosci Lett 367:394–398.

Perrenoud Q, Pennartz CMA, Gentet LJ (2016) Membrane potential dynamics of spontaneous and visually evoked gamma activity in V1 of awake mice. PLoS Biol 14:e1002383–21.

Petersen CCH (2014) Cortical control of whisker movement. Annu Rev Neurosci 37:183–203.

Petersen CCH (2019) Sensorimotor processing in the rodent barrel cortex. Nat Rev Neurosci 20:533–546.

Peyrache A, Battaglia FP, Destexhe A (2011) Inhibition recruitment in prefrontal cortex during sleep spindles and gating of hippocampal inputs. Proc Natl Acad Sci USA 108:17207–17212.

Pfeffer CK, Xue M, He M, Huang ZJ, Scanziani M (2013) Inhibition of inhibition in visual cortex: the logic of connections between molecularly distinct interneurons. Nat Neurosci 16:1068–1076.

Prönneke A, Witte M, Möck M, Staiger JF (2020) Neuromodulation leads to a burst-tonic switch in a subset of VIP neurons in mouse primary somatosensory (Barrel) cortex. Cereb Cortex 30:488–504.

Steriade M, Timofeev I (2003) Neuronal plasticity in thalamocortical networks during sleep and waking oscillations. Neuron 37:563–576.

Steriade M, Timofeev I, Grenier F (2001) Natural waking and sleep states: a view from inside neocortical neurons. J Physiol 85:1969–1985.

Takahashi K, Lin JS, Sakai K (2006) Neuronal activity of histaminergic tuberomammillary neurons during wake-sleep states in the mouse. J Neurosci 26:10292–10298.

Taniguchi H, He M, Wu P, Kim S, Paik R, Sugino K, Kvitsiani D, Fu Y, Lu J, Lin Y, Miyoshi G, Shima Y, Fishell G, Nelson SB, Huang ZJ (2011) A resource of Cre driver lines for genetic targeting of GABAergic neurons in cerebral cortex. Neuron 71:995–1013.

Tiriac A, Uitermarkt BD, Fanning AS, Sokoloff G, Blumberg MS (2012) Rapid whisker movements in sleeping newborn rats. Curr Biol 22:2075–2080.

Todorova R, Zugaro M (2019) Isolated cortical computations during delta waves support memory consolidation. Science 366:377–381.

Tononi G, Cirelli C (2009) Sleep and the price of plasticity: from synaptic to cellular homeostasis to memory consolidation and integration. Neuron 49:1841–1850.

Tremblay R, Lee S, Rudy B (2016) GABAergic interneurons in the neocortex: from cellular properties to circuits. Neuron 91:260–292.

Ulrich D (2016) Sleep spindles as facilitators of memory formation and learning. Neural Plast. Advance online publication. Retrieved March 28, 2016. doi: 10.1155/2016/1796715.

Urbain N, Fourcaud-Trocmé N, Laheux S, Salin PA, Gentet LJ (2019) Brain-state-dependent modulation of neuronal firing and membrane potential dynamics in the somatosensory thalamus during natural sleep. Cell Rep 26:1443–1457.e5.

van Dongen EV, Takashima A, Barth M, Fernández G (2011) Functional connectivity during light sleep is correlated with memory performance for face-location associations. Neuroimage 57:262–270.

Vaz AP, Wittig JH, Inati SK, Zaghloul KA (2020) Replay of cortical spiking sequences during human memory retrieval. Science 367:1131–1134.

Velluti RA (1997) Interactions between sleep and sensory physiology. J Sleep Res 6:61–77.

Vijayan S, Hale GJ, Moore CI, Brown EN, Wilson M (2010) Activity in the barrel cortex during active behavior and sleep. J Neurophysiol 103:2074–2084.

Vinck M, Bos JJ, van Mourik-Donga LA, Oplaat KT, Klein GA, Jackson JC, Gentet LJ, Pennartz CMA (2016) Cell-type and state-dependent synchronization among rodent somatosensory, visual, perirhinal cortex, and hippocampus CA1. Front Syst Neurosci 9:187.

Vyazovskiy VV, Olcese U, Lazimy YM, Faraguna U, Esser SK, Williams JC, Cirelli C, Tononi G (2009) Cortical firing and sleep homeostasis. Neuron 63:865–878.

Watson BO, Levenstein D, Greene JP, Gelinas JN, Buzsáki G (2016) Network homeostasis and state dynamics of neocortical sleep. Neuron 90:839–852.

Welker WI (1964) Analysis of sniffing of the albino rat. Behav 22:223–244.

Yu J, Hu H, Agmon A, Svoboda K (2019) Recruitment of GABAergic interneurons in the barrel cortex during active tactile behavior. Neuron 104:412–427.